Volume 2
Number 20
21 October 2021
Pages 6457–6734

Materials Advances

rsc.li/materials-advances

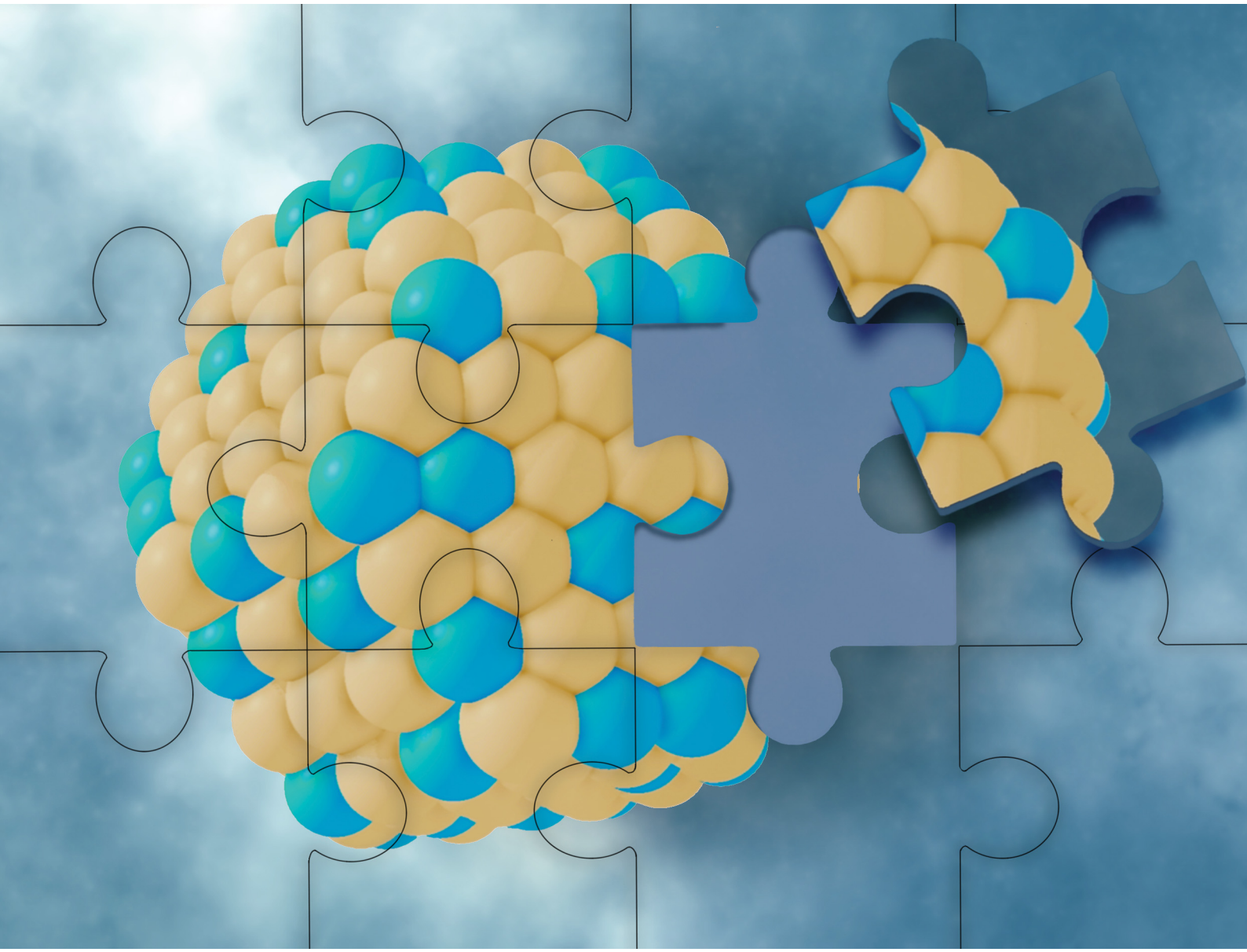

ISSN 2633-5409

ROYAL SOCIETY OF CHEMISTRY

PAPER

Hristiyan A. Aleksandrov, Konstantin M. Neyman *et al.*
Chemical ordering in Pt–Au, Pt–Ag and Pt–Cu nanoparticles from density functional calculations using a topological approach

Materials Advances

ROYAL SOCIETY OF CHEMISTRY

PAPER

View Article Online
View Journal | View Issue

Cite this: *Mater. Adv.*, 2021, 2, 6589

Chemical ordering in Pt–Au, Pt–Ag and Pt–Cu nanoparticles from density functional calculations using a topological approach†

Lorena Vega,[a] Hristiyan A. Aleksandrov, *[b] Riccardo Farris,[a] Albert Bruix, [a] Francesc Viñes [a] and Konstantin M. Neyman *[ac]

Bimetallic alloys are actively investigated as promising new materials for catalytic and other energy-related applications. However, the stable arrangements of the two metals in prevailing nanostructured systems, which define their structure and surface reactivity, are seldom addressed. The equilibrium chemical orderings of bimetallic nanoparticles are usually different from those in the corresponding bulk phases and hard to control experimentally, which hampers assessment of the relations between composition, structure, and reactivity. Herewith, we study mixtures of platinum—an essential metal in catalysis—alloyed with coinage metals gold, silver, and copper. These systems are interesting, for instance, for reducing the costly Pt content and designing improved multifunctional catalysts, but the chemical orderings in such mixtures at the nanoscale are still debated. We therefore explore chemical orderings and properties of Pt-containing nanoalloys by means of a topological method based on density functional calculations. We determine the lowest-energy chemical orderings in 1.4 to 4.4 nm large Pt–Au, Pt–Ag and Pt–Cu particles with different contents of metals. Chemical ordering, bonding, and charge distribution in the nanoparticles are analyzed, identifying how peculiar structural motifs relevant for catalysis and sensing applications, such as monometallic skins and surface single-atom sites, emerge. We compare these results with previous data for the corresponding Pd-based particles, identifying trends in chemical ordering, deepening understanding of the behaviour of catalytically relevant bimetallic compositions, and establishing appropriate models for studying the bimetallic nanoalloys.

Received 17th June 2021,
Accepted 4th August 2021

DOI: 10.1039/d1ma00529d

rsc.li/materials-advances

1. Introduction

Studies of materials containing bimetallic nanoparticles (NPs), often referred to as nanoalloys, is a dynamically developing research area. The latter is interrelated to diverse applications of nanoalloy particles ranging from optics and magnetism to medicine and catalysis.[1,2] Properties of a bimetallic NP are defined, besides its geometric structure and size, by the relative amount (composition) of the two constituting metals. Tuning the composition extends the design variables of materials containing bimetallic NPs tailor-made for the desired applications to function better, often at reduced cost.

The size, shape, and composition of bimetallic NPs can be quite well controlled by the preparation conditions. At variance, such elusive degree of complexity as chemical (or atomic) ordering, *i.e.* a distribution pattern of metal atoms of two types among lattice positions of an alloy NP, is hard to precisely control experimentally. The reactivity of metal NPs is directly related to their surface arrangement. The chemical ordering defines what types and how many surface sites are exposed by a bimetallic NP of a given size, shape, and composition. This is key information for catalysis, sensing, and many other applications. Yet, it remains barely accessible experimentally at the atom-by-atom level even for the most modern structure characterization techniques.

Computational modeling using Density Functional Theory (DFT) can provide detailed information about the structure and properties of bimetallic NPs, complementing experimental data. DFT calculations of bimetallic NPs with over a hundred atoms and sizes of ~1.5 nm, which are required to realistically

[a] *Departament de Ciència de Materials i Química Física & Institut de Química Teòrica i Computacional (IQTCUB), Universitat de Barcelona, 08028 Barcelona, Spain*
[b] *Faculty of Chemistry and Pharmacy, University of Sofia, 1126 Sofia, Bulgaria. E-mail: haa@chem.uni-sofia.bg*
[c] *ICREA (Institució Catalana de Recerca i Estudis Avançats), 08010 Barcelona, Spain. E-mail: konstantin.neyman@icrea.cat*

† Electronic supplementary information (ESI) available: Structural and energy data calculated by DFT of the discussed in the article Pt–Au, Pt–Ag and Pt–Cu nanoparticles (PDF). See DOI: 10.1039/d1ma00529d

represent larger particles dealt with in catalysis,[3–5] are feasible since two decades.[6] However, the presence of more than one type of atoms in nanoalloys severely hinders their comprehensive DFT simulation, often restricting it to quite small particles and considering only several chemical orderings (homotops).[7–12] In fact, a direct search for the equilibrium chemical ordering in a ~2 nm large bimetallic crystallite comprising ~200 atoms requires calculating energies of a colossal number of 10^{50} homotops (including symmetry-equivalent ones),[13] which is excessive for any computational method.

This challenge can be dealt with by a Topological (TOP) approach,[14,15] which enables determining equilibrium chemical orderings in bimetallic nanocrystallites containing 10^2–10^4 atoms of different metals across the Periodic Table from a small number of DFT calculations. Briefly, the TOP method divides all homotops of a bimetallic nanocrystallite with a given stoichiometry and shape into groups with the same topologies. Definition of the latter depends on how atomically detailed the resulting ordering needs to be. For instance, for studying the catalytic activity of a bimetallic M'_mM_n NP comprising $m + n$ atoms it is essential to know how many active surface sites of each type the NP exposes. These data are related to the propensity of M′ and M atoms to segregate on the surface and define which atoms occupy surface positions of the NP with different coordination numbers, *e.g.* in corner, edge, and terrace sites. Since all homotops of the NP under scrutiny share the same crystal lattice and composition, it suffices to specify atomic positions for just one of the two metals. The types of the exposed surface sites and their abundance are also affected by the propensity of the metals M′ and M to mix, which is reflected by the number of heterometallic bonds (nearest-neighbor atom pairs) M′–M formed. For surface reactivity studies it is often sufficient to specify ordering patterns in bimetallic nanoalloys by the topology defined solely by the number of M′–M bonds $\left(N_{\mathrm{BOND}}^{\mathrm{M'-M}}\right)$ and surface M atoms in the corner/vertex ($N_{\mathrm{CORNER}}^{\mathrm{M}}$), edge ($N_{\mathrm{EDGE}}^{\mathrm{M}}$), and facet/terrace ($N_{\mathrm{FACET}}^{\mathrm{M}}$) positions. Hereafter, topologies of M'_mM_n NPs are designated as $M'_mM_n\_N_{\mathrm{BOND}}^{\mathrm{M'-M}} \cdot N_{\mathrm{CORNER}}^{\mathrm{M}} \cdot N_{\mathrm{EDGE}}^{\mathrm{M}} \cdot N_{\mathrm{FACET}}^{\mathrm{M}}$; to specify a particular homotop of the considered topology, its E^{DFT} value in eV is added to the above designation, resulting in the designation $M'_mM_n\_N_{\mathrm{BOND}}^{\mathrm{M'-M}} \cdot N_{\mathrm{CORNER}}^{\mathrm{M}} \cdot N_{\mathrm{EDGE}}^{\mathrm{M}} \cdot N_{\mathrm{FACET}}^{\mathrm{M}} E^{\mathrm{DFT}}$. Energies of all homotops with a given topology are represented in the TOP method by the energy of just one of the homotops, chosen arbitrarily.[14]

Energy difference, $\Delta E_{ij}^{\mathrm{TOP}}$, between any two homotops i and j of a bimetallic NP reads:[14,16]

$$\begin{aligned}\Delta E_{ij}^{\mathrm{TOP}} &= E_j^{\mathrm{TOP}}\left(N_{j,\mathrm{BOND}}^{\mathrm{M'-M}}, N_{j,\mathrm{CORNER}}^{\mathrm{M}}, N_{j,\mathrm{EDGE}}^{\mathrm{M}}, N_{j,\mathrm{FACET}}^{\mathrm{M}}\right) \\ &\quad - E_i^{\mathrm{TOP}}\left(N_{i,\mathrm{BOND}}^{\mathrm{M'-M}}, N_{i,\mathrm{CORNER}}^{\mathrm{M}}, N_{i,\mathrm{EDGE}}^{\mathrm{M}}, N_{i,\mathrm{FACET}}^{\mathrm{M}}\right) \\ &= \varepsilon_{\mathrm{BOND}}^{\mathrm{M'-M}} \cdot \Delta N_{ij,\mathrm{BOND}}^{\mathrm{M'-M}} + \varepsilon_{\mathrm{CORNER}}^{\mathrm{M}} \cdot \Delta N_{ij,\mathrm{CORNER}}^{\mathrm{M}} \\ &\quad + \varepsilon_{\mathrm{EDGE}}^{\mathrm{M}} \cdot \Delta N_{ij,\mathrm{EDGE}}^{\mathrm{M}} + \varepsilon_{\mathrm{FACET}}^{\mathrm{M}} \cdot \Delta N_{ij,\mathrm{FACET}}^{\mathrm{M}}\end{aligned} \quad (1)$$

with $\Delta N_{ij} = N_j - N_i$.

Here, the energies ε are contributions of either a M′–M bond or an M atom located in a certain outer position of the NP to its topological energy E^{TOP}. The terms ε quantify either the surface segregation energy of metal atoms M′ and M or the energy gained or lost upon metals mixing to form a pair M′–M of the nearest-neighbor atoms. These terms are calculated by fitting eqn (1) to DFT energies E^{DFT} of a series of homotops of a bimetallic NP with diverse topologies. Using thus obtained TOP expressions a comprehensive ordering screening is performed by means of Monte Carlo (MC) simulations to find the topology—a set of the N values—of the most energetically stable homotops of the NP along with topologies of less stable homotops. Then, atomic positions in the selected low-energy homotops are optimized by DFT. This allows examining accuracy of the energies ε and eqn (1) overall. The resulting latter expressions can be used to simulate the chemical orderings in bimetallic NPs containing thousands atoms, not accessible for DFT calculations.

Successfully determined chemical orderings in NPs of various metal combinations, such as Pd–Au,[13–17] Pd–Ag,[14] Pd–Cu,[14] Pd–Zn,[14] Pd–Rh,[16] Pt–Ag,[18] Pt–Co,[19,20] Pt–Ni,[21] Pt–Sn,[22] and Ni–Cu,[23] revealed efficiency and broad applicability of the TOP method. This study deals with bimetallic nanoalloys of essential for catalysis metal Pt with quite inert coinage metals Au, Ag, and Cu. These combinations of metals are actively studied in the rapidly developing field of single-atom catalysis[24,25] as single-atom alloy catalysts,[26] where individual Pt atoms surrounded by coinage atoms can act as very selective catalytic centers.

Among the aims of the present study are:(i) quantifying by DFT calculations the chemical orderings and surface segregation in up to ~2 nm large Pt–Au, Pt–Ag and Pt–Cu crystallites at different concentrations of the metals; (ii) analyzing the structure, bonding, and atomic charges in these nanoparticles compared to the analogous Pd-containing nanoalloys studied earlier; (iii) deepening the knowledge of the accuracy and applicability of the Topological approach; (iv) identifying equilibrium chemical orderings in Pt–Au, Pt–Ag and Pt–Cu particles at sizes over 4 nm commonly found in catalysts, also at elevated temperatures.

2. Computational methods

All DFT calculations were performed using the plane-wave code VASP.[27,28] A gradient-corrected Perdew–Burke–Ernzerhof (PBE) exchange–correlation functional[29] was employed as one of the most reliable functionals for transition metals bulks and surfaces[30–32] in combination with the projector augmented wave (PAW) representation of core electrons.[33,34] Insignificant spin-polarization effects for the non-magnetic platinum and coinage metals were neglected. To moderate the computational cost, cutoff energies for the plane-wave functions were defined by the values of the PBE core-electrons PAW potentials:Cu – 273.2 eV, Ag – 249.85 eV, Au – 229.95 eV and Pt – 230.28 eV. According to our benchmarks, the total energy differences between distinct chemical orderings of a given NP computed using these cutoff energies are essentially as accurate as when

using the cutoff energy 415 eV (typically used for describing adsorbate–metal interactions). The Brillouin zone was sampled only at the Γ-point. One-electron Kohn–Sham levels were smeared by 0.1 eV and the converged energies were finally extrapolated to zero smearing. All atoms were locally relaxed without any restrictions until forces acting on each atom decreased to 0.2 eV nm^{-1}.

In line with our DFT calculations of other nanoalloy particles,[13,14,16,21] here the Pt–X (X = Au, Ag, Cu) NPs were also represented by truncated octahedrons with the fcc lattice. *Ca.* 1.4 nm large 140-atomic $Pt_{70}Au_{70}$, $Pt_{70}Ag_{70}$, and $Pt_{70}Cu_{70}$ NPs, see Fig. 1, were considered for comparison with the results for Pd-based $Pd_{70}Au_{70}$, $Pd_{70}Ag_{70}$, and $Pd_{70}Cu_{70}$ analogs.[14] 1.7–1.8 nm large 201-atomic NPs Pt–Au, Pt–Ag and Pt–Cu with Pt : X 1 : 3, 1 : 1, and 3 : 1 compositions, see Fig. 2, were modelled to study the size, shape, and composition effects. Placing these 140- and 201-atom NPs in periodically repeated cubic cells of 2.3 × 2.3 × 2.3 and 2.5 × 2.5 × 2.5 nm^3 allowed separation >0.7 nm between them. At such distances interaction of metal particles with their periodic images is negligible for the purpose of this work.[35,36]

3. Results and discussion

In the following we present and discuss results for model Pt–X (X = Au, Ag, Cu) NPs $Pt_{51}X_{150}$ (1 : 3), $Pt_{101}X_{100}$ (1 : 1), $Pt_{151}X_{50}$ (3 : 1), and $Pt_{70}X_{70}$ (1 : 1). These fcc crystallites expose surface atoms with the coordination numbers (CN) 6 (corner/vertex), 7 (edge), and 9 ({111} facets). Besides, the 201-atomic particles contain one atom with CN = 8 in each of their six {100} facets. Table 1 shows the calculated energy terms ε in the topological expressions (eqn (1)). Details of the lowest-energy chemical orderings resulting from DFT calculations (E^{DFT}) and from MC calculations using eqn (1) (E^{TOP}) are specified in Table 2. These two kinds of chemical orderings are quite similar for each studied model NP. Thus, unless stated otherwise, herein we consider the chemical orderings corresponding to the E^{TOP} values.

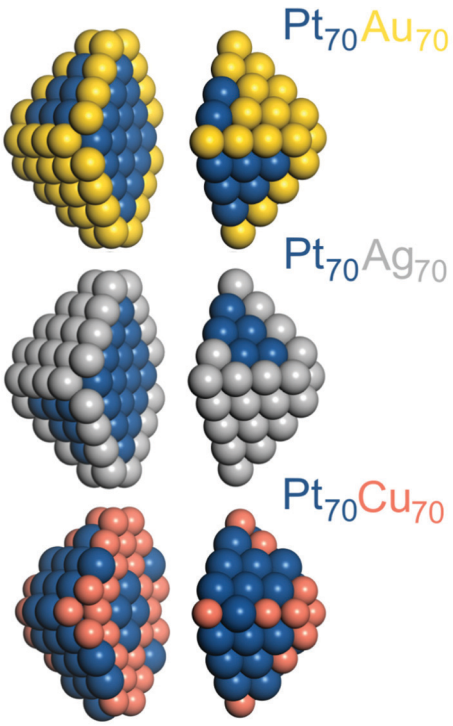

Fig. 1 Chemical orderings of *ca.* 1.4 nm large 140-atomic truncated-octahedral fcc nanoparticles $Pt_{70}Au_{70}$, $Pt_{70}Ag_{70}$, and $Pt_{70}Cu_{70}$ with the lowest DFT energies. Particles images are split in two parts for better visualization. Pt – blue, Au – yellow, Ag – gray, Cu – red-brown.

The following literature data are relevant for the present study of the Pt–X nanoalloys:(i) the surface energies calculated for close-packed surfaces of the pure metals are 1.03 (Pt), 0.72 (Au), 0.58 (Ag), and 0.77 eV per atom (Cu);[37] (ii) calculated solutes/hosts surface segregation energies of monoatomic impurities (solutes) in fcc(111) metal hosts are −0.36 (Au/Pt), 0.34 (Pt/Au), −0.27 (Ag/Pt), 0.34 (Pt/Ag), 0.32 (Cu/Pt), and −0.04 eV (Pt/Cu), where the negative sign indicates stabilizing surface segregation of the solute;[37] (iii) Pt atoms in the bulk alloys are immiscible with Au[38–41] and Ag[40] atoms, but miscible with Cu[40,42–44] atoms; and (iv) relative sizes of metal atoms,[45] 139 (Pt), 144 (Au), 144 (Ag), and 128 pm (Cu), affect the propensity of smaller atoms to surface segregate in compressively strained bimetallic particles[40,46–48] so that the surface segregation of Cu is suppressed in Pt–Cu nanoalloys despite Cu has a lower surface energy than Pt (see above).

3.1. DFT data for chemical orderings of Pt–Au nanoparticles

$Pt_{51}Au_{150}$, $Pt_{101}Au_{100}$, and $Pt_{151}Au_{50}$ nanoparticles. Calculated data for 201-atomic Pt–Au NPs with the Pt : Au compositions 1 : 3, 1 : 1, and 3 : 1, see Tables 1, 2 and Fig. 2, reveal that their chemical orderings are controlled, in agreement with the data for Pt–Au bulk, surface, and nanoalloys,[37–40] by the following effects:first, the positive energies $\varepsilon^{Pt\text{-}Au}_{BOND}$ = 15–21 meV (Table 1) indicate that the formation of Pt–Au bonds in the alloys is disfavored with respect to Pt–Pt and Au–Au bonds, suppressing mixing of Pt and Au atoms. Second, quite large in magnitude negative terms $\varepsilon^{Au}_{CORNER}$ = −507 to −558 meV, ε^{Au}_{EDGE} = −492 to −547 meV and ε^{Au}_{FACET} = −259 to −431 meV show that Au atoms are notably more stable on the surface of the NPs than inside them and thus segregate on the surface. More open corner and edge Au atoms are more stable than higher-coordinated facet Au atoms. Increase of ε^{Au}_{FACET} in magnitude with increasing Pt : Au content from 1 : 3 to 1 : 1, and to 3 : 1 suggests that the location of Pt atoms in facets of Pt–Au NPs is less energetically penalized at lower Pt concentrations than at higher ones. The surface segregation of Au atoms in the 201-atomic Pt–Au NPs with the lowest-energy orderings is illustrated in Fig. 2 and additionally detailed in Table 2 by numbers of atoms in various sites. Au atoms of $Pt_{51}Au_{150}$ occupy all 24 corner, 36 edge, and 62 facet sites forming a complete monolayer Au skin. The remaining 28 Au atoms are located inside, tending to minimize the number of unfavorable Pt–Au nearest-neighbor contacts. $Pt_{101}Au_{100}$ NP has insufficient Au atoms to complete the Au skin. There, 100 Au atoms occupy

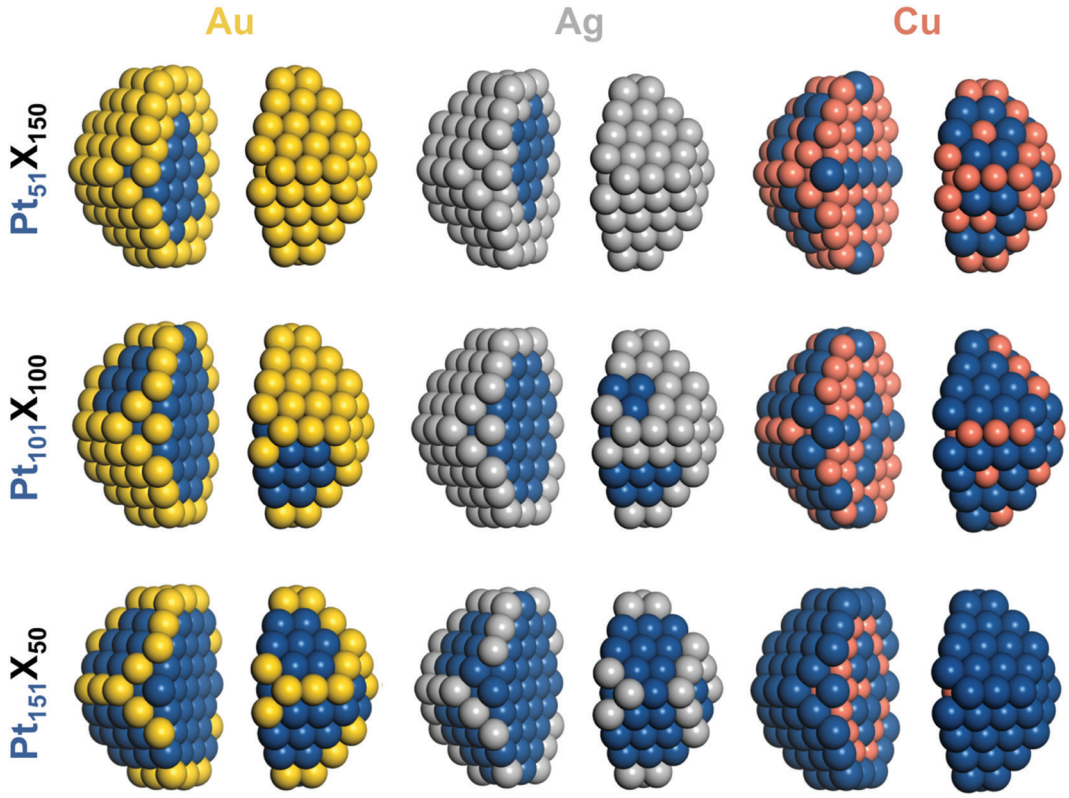

Fig. 2 Chemical orderings of 1.7–1.8 nm large 201-atomic truncated-octahedral fcc nanoparticles of the compositions Pt:X (X = Au, Ag, Cu):1: 3 – $Pt_{51}X_{150}$, 1:1 – $Pt_{101}X_{100}$, 3:1 – $Pt_{151}X_{50}$ with the lowest DFT energies. Particles images are split in two parts for better visualization. Colors of atoms as in Fig. 1.

all 24 corner and 36 edge surface sites plus 40 of 62 facet sites. Even fewer Au atoms in $Pt_{151}Au_{50}$ NP results in their competition to partly occupy only corner and edge sites.

The usefulness of the TOP approach and the meaning of terms in eqn (1) can be illustrated by comparing the TOP and DFT segregation energies. A homotop of $Pt_{51}Au_{150}$ with almost lowest TOP energy, $Pt_{51}Au_{150}$_212.24.36.62–729.864 (see ESI†), is characterized by $N_{BOND}^{Pt\text{-}Au} = 212$, $N_{CORNER}^{Au} = 24$, $N_{EDGE}^{Au} = 36$ and $N_{FACET}^{Au} = 62$ and $E^{DFT} = -729.864$ eV (homotops are labeled in this way throughout the present article). Exchange of an atom Au from center of a {111} facet with a near-neighbor subsurface atom Pt (each of the exchanged atoms Au number 39 and Pt number 198 formed 3 Pt–Au bonds) results in the homotop $Pt_{51}Au_{150}$_223.24.36.61–729.507 (see ESI†), where, the surface Pt atom forms 7 Pt–Au bonds and the Au atom moved to the subsurface forms 10 Pt–Au bonds. Its energy increase with respect to the pristine homotop is $\Delta E^{TOP} = \varepsilon_{BOND}^{Pt-Au}\Delta N_{BOND}^{Pt-Au} + \varepsilon_{FACET}^{Au}\Delta N_{FACET}^{Au} = 11 \times 15$ meV + 259 meV = 424 meV, using eqn (1) and energies ε in Table 1. The DFT energy increase 357 meV is close to the ΔE^{TOP} value in terms of the precision $\delta(E^{DFT} - E^{TOP}) = 279$ meV (Table 1). $\delta(E^{DFT} - E^{TOP})$ is twice the residual standard deviation between E^{DFT} and E^{TOP} energies for homotops of $\geq$10 test low-energy topologies, according to which the respective ΔE^{TOP} and ΔE^{DFT} values differ by less than δ with the probability $\geq$95%.[14] Exchange of an edge atom Au with a nearby subsurface atom Pt in the pristine homotop models even less favorable surface segregation of inner atoms Pt to edge sites. $N_{BOND}^{Pt\text{-}Au}$ after this exchange of atom Au number 132 with atom Pt number 176 (see ESI†) increases in the resulting homotop $Pt_{51}Au_{150}$_219.24.35.62–729.345 for the atom Au from 1 to 6 and for the atom Pt from 5 to 7. The energy increase *vs.* the pristine homotop, $\Delta E^{TOP} = \varepsilon_{BOND}^{Pt-Au}\Delta N_{BOND}^{Pt-Au} + \varepsilon_{EDGE}^{Au}\Delta N_{EDGE}^{Au} = 7 \times 15$ meV + 547 meV = 652 meV, is indeed larger than for the displacement of the inner atom Pt to a {111} facet and reasonably well agrees with $\Delta E^{DFT} = 519$ meV.

These two examples demonstrate that the TOP method, beyond providing adequate relative energies of different chemical orderings of a bimetallic NP, also allows rationalizing the energy differences in such important terms as propensities of their two types of metal atoms to form heterometallic bonds and to occupy differently coordinated surface sites.

$Pt_{70}Au_{70}$ nanoparticle. The size-sensitivity of the interactions governing equilibrium orderings in Pt–Au NPs at a given Pt:Au composition can be explored by comparing the ordering of the $Pt_{101}Au_{100}$ particle with that of the smaller $Pt_{70}Au_{70}$ particle sketched in Fig. 1. One can see from Table 1 that $\varepsilon_{BOND}^{Pt\text{-}Au} = 19$ meV for $Pt_{70}Au_{70}$ remains within the error bar of the same quantity for $Pt_{101}Au_{100}$, indicating that quite low immiscibility of Pt and Au atoms is almost independent of the particle size in this size range. Surface segregation of Au atoms is strongly energetically preferred also in the $Pt_{70}Au_{70}$ particle. There, the energy gain by displacement of an inner atom Au to a corner without changing the number of Pt–Au bonds (*i.e.* $\varepsilon_{CORNER}^{Au}$) is 619 meV, exceeding that for $Pt_{101}Au_{100}$ particle, 530 meV. At

Table 1 Energy terms,[a] ε, in the topological expressions[14,15] (eqn (1)) for energy differences ΔE_{ij}^{TOP} of homotops i and j of Pt_nX_m (X = Au, Ag, Cu; $m + n = 140, 201$) particles $\Delta E_{ij}^{TOP} = \varepsilon_{BOND}^{Pt\text{-}X}\cdot\Delta N_{ij,BOND}^{Pt\text{-}X} + \varepsilon_{CORNER}^{X}\cdot\Delta N_{ij,CORNER}^{X} + \varepsilon_{FACET}^{X}\cdot\Delta N_{ij,FACET}^{X}$. Here, $\Delta N_{ij} = N_j - N_i$, $N_{BOND}^{Pt\text{-}X}$, N_{CORNER}^{X}, N_{EDGE}^{X}, N_{FACET}^{X}, are numbers of heterometallic bonds Pt–X (nearest-neighbor pairs of Pt–X atoms) and atoms X in the corner (vertex), edge and facet positions of the particle, respectively. The $\delta(E^{DFT} - E^{TOP})^b$ and ΔE (calculated using E^{TOP}) are precision and accuracy values, respectively.[14] All energies are in meV. N_{FIT} is the number of homotops calculated by DFT for each NP used to fit the TOP expressions. Data for analogous $Pd_{70}Au_{70}$, $Pd_{70}Ag_{70}$, and $Pd_{70}Cu_{70}$ particles from ref. 14 are also shown

Nanoparticle	$\varepsilon_{BOND}^{Pt\text{-}X}$	ε_{CORNER}^{X}	ε_{EDGE}^{X}	ε_{FACET}^{X}	δ	ΔE	N_{FIT}
$Pt_{70}Au_{70}$	19^{+4}_{-2}	-619^{+62}_{-48}	-377^{+44}_{-44}	-256^{+88}_{-69}	470	0	35
$Pd_{70}Au_{70}$	-13^{+4}_{-6}	-404^{+76}_{-72}	-301^{+52}_{-77}	-200^{+52}_{-64}	115	26	32
$Pt_{70}Ag_{70}$	11^{+10}_{-13}	-625^{+122}_{-185}	-336^{+72}_{-185}	-195^{+75}_{-58}	358	0	45
$Pd_{70}Ag_{70}$	-1^{+2}_{-2}	-361^{+50}_{-68}	-289^{+78}_{-129}	-163^{+43}_{-64}	150	29	53
$Pt_{70}Cu_{70}$	-35^{+4}_{-4}	-27^{+47}_{-44}	182^{+56}_{-54}	344^{+43}_{-36}	879	415	65
$Pd_{70}Cu_{70}$	-26^{+5}_{-5}	95^{+36}_{-33}	147^{+46}_{-45}	183^{+42}_{-40}	360	171	127
$Pt_{151}Au_{50}$	21^{+1}_{-1}	-507^{+51}_{-62}	-543^{+16}_{-18}	-431^{+30}_{-43}	114	354	101
$Pt_{101}Au_{100}$	21^{+7}_{-6}	-530^{+136}_{-107}	-492^{+59}_{-56}	-335^{+83}_{-95}	456	0	68
$Pt_{51}Au_{150}$	15^{+14}_{-15}	-558^{+49}_{-34}	-547^{+53}_{-84}	-259^{+47}_{-92}	279	198	44
$Pt_{151}Ag_{50}$	32^{+11}_{-12}	-396^{+108}_{-135}	-380^{+95}_{-90}	-237^{+103}_{-95}	461	176	90
$Pt_{101}Ag_{100}$	16^{+9}_{-10}	-499^{+95}_{-112}	-466^{+87}_{-83}	-308^{+77}_{-91}	493	65	68
$Pt_{51}Ag_{150}$	7^{+5}_{-5}	-408^{+118}_{-158}	-511^{+79}_{-68}	-240^{+49}_{-65}	169	43	99
$Pt_{151}Cu_{50}$	-25^{+9}_{-13}	267^{+30}_{-22}	342^{+14}_{-14}	372^{+42}_{-44}	784	204	165
$Pt_{101}Cu_{100}$	-43^{+6}_{-5}	15^{+60}_{-72}	208^{+55}_{-68}	325^{+34}_{-41}	576	284	87
$Pt_{51}Cu_{150}$	-54^{+14}_{-15}	134^{+73}_{-78}	184^{+151}_{-93}	259^{+65}_{-59}	239	0	40

[a] 95% confidence interval of ε given as, *e.g.* 19^{+4}_{-2} denotes a range from 17 meV to 23 meV. [b] When several homotops were optimized by DFT for one of the selected $\geq$10 low-energy topologies, see Section 3.6, all these E^{DFT} values were also used in the calculations of δ.

variance, the energy gained by the relocation of an inner Au atom to edges and terraces (*i.e.* ε_{EDGE}^{Au} and ε_{FACET}^{Au}) is 377 and 256 meV, respectively, smaller than for $Pt_{101}Au_{100}$ particle, 492 and 335 meV. These findings indicate that Au atoms are better distributed between low-coordinated (corner, edge) positions and higher-coordinated terrace positions in larger 1:1 Pt–Au particles than in smaller ones, where Au clearly prefers corners. The lowest-energy topology of the $Pt_{70}Au_{70}$ particle, see Table 2, corresponds to complete occupation of all 24 corner and 24 edge sites by Au atoms and location of all remaining 22 Au atoms on the facets. The percentage of 196 Pt–Au bonds in $Pt_{70}Au_{70}$, 31% of all metal–metal bonds, is comparable to 28% of 267 Pt–Au bonds in $Pt_{101}Au_{100}$. Some $Pt_{70}Au_{70}$ results will be further discussed in the sections dealing with the comparison of Pt–X NPs with their Pd–X analogs as well as with predicting chemical orderings in larger Pt–X NPs, where DFT calculations are unfeasible.

Charge distribution. Only a minor charge redistribution occurs between Pt and Au atoms in Pt–Au NPs. According to the Bader charge analysis, see Table 3, for most of surface Pt and Au atoms in Pt–Au nanoalloys the average charges are within 0.03 $|e|$ of the charges calculated in the corresponding surface positions of the monometallic Pt_{201} and Au_{201} particles. (Note that in the monometallic particles Bader charges of surface atoms are slightly negative and grow in magnitude with decreasing coordination numbers.) These data suggest a close similarity of the adsorption and reactivity properties of pure Pt and Au surface sites in Pt–Au NPs with the corresponding surface sites in monometallic Pt and Au NPs.

3.2. DFT data for chemical orderings of Pt–Ag nanoparticles

$Pt_{51}Ag_{150}$, $Pt_{101}Ag_{100}$, and $Pt_{151}Ag_{50}$ nanoparticles. Data defining orderings in Pt–Ag NPs, see Tables 1, 2 and Fig. 2, resemble the data for the Pt–Au NPs. In particular, slightly positive energies $\varepsilon_{BOND}^{Pt\text{-}Ag}$ (Table 1) reveal disfavoured mixing of Pt and Ag atoms with the formation of the Pt–Ag bonds, similar to the Pt–Au bonds. This propensity of Pt and Ag components to stay separate is counteracted in NPs by 380–510 meV strong stabilization of Ag atoms in low-coordinated surface corner and edge positions. The stabilization of Ag atoms in surface terrace (facet) positions is somewhat weaker, but still significant, 240–310 meV.

Ordering of the lowest-energy homotops of $Pt_{101}Ag_{100}$ NP is very similar to those of $Pt_{101}Au_{100}$ NP, see Fig. 2 and Table 2. All Ag atoms are located on the surface occupying all 24 corner and 36 edge sites and 40 of 62 terrace sites. Pt atoms occupy the remaining terrace sites and all 79 inner sites. This ordering exhibits incomplete Ag outer shell and monometallic Pt core. Qualitatively the same values of energies ε guiding the orderings in 201-atom NPs with other Pt:Ag ratios, $Pt_{51}Ag_{150}$, and

Table 2 Numbers of Pt–X bonds and atoms X = Au, Ag, Cu in various positions with the coordination numbers 6 – corner/vertex, 7 – edge, 8 + 9 – {100} + {111} facets, and 8 – {100} facets in the lowest-energy homotops of the $Pt_{70}X_{70}$, $Pt_{151}X_{50}$, $Pt_{101}X_{100}$, and $Pt_{51}X_{150}$ particles optimized at DFT/TOP levels along with DFT energies of these homotops, E_{DFTmin}^{DFT} and E_{TOPmin}^{DFT}, respectively[a]

Particle	$N_{BOND}^{Pt\text{-}X}$	N_{CORNER}^{X}	N_{EDGE}^{X}	N_{FACET}^{X}	N_{100}^{X}	E_{DFTmin}^{DFT} (eV)	E_{TOPmin}^{DFT} (eV)
$Pt_{70}Au_{70}$	196/196	24/24	24/24	22/22		−588.108	−588.108
$Pt_{70}Ag_{70}$	196/196	24/24	24/24	22/22		−561.294	−561.294
$Pt_{70}Cu_{70}$	308/340	23/24	8/12	0/0		−626.920	−626.610
$Pt_{151}Au_{50}$	215/214	23/20	25/30	2/0	2/0	−978.389	−978.283
$Pt_{151}Ag_{50}$	222/215	24/21	26/29	0/0	0/0	−962.454	−961.772
$Pt_{151}Cu_{50}$	404/412	0/0	0/0	0/0	0/0	−1015.683	−1015.214
$Pt_{101}Au_{100}$	267/267	24/24	36/36	40/40	5/5	−859.505	−859.505
$Pt_{101}Ag_{100}$	274/270	24/24	36/36	40/40	6/4	−822.032	−821.660
$Pt_{101}Cu_{100}$	525/560	24/24	10/8	3/8	0/0	−914.377	−913.767
$Pt_{51}Au_{150}$	224/210	24/24	36/36	62/62	6/6	−730.046	−729.869
$Pt_{51}Ag_{150}$	220/214	24/24	36/36	62/62	6/6	−669.026	−668.827
$Pt_{51}Cu_{150}$	418/418	24/24	36/36	18/18	0/0	−799.627	−799.627

[a] The overall topological numbers N_{BOND}, N_{CORNER}, N_{EDGE}, N_{FACET}, and N_{INSIDE} are 636, 24, 24, 48, 44 ($Pt_{70}X_{70}$), and 948, 24, 36, 62, 79 ($Pt_{201-n}X_n$), respectively.

Table 3 Average Bader charges, in |e|, on atoms with coordination numbers 6, 7, 8, 9, 12 in $Pt_{70}X_{70}$, $Pt_{151}X_{50}$, $Pt_{101}X_{100}$, and $Pt_{51}X_{150}$ (X = Au, Ag, Cu) NPs with the lowest E^{TOP} energy. The charges in the monometallic Pt_{201} and X_{201} NPs are also shown for comparison

	Pt					X				
Particle	6	7	8	9	12	6	7	8	9	12
$Pt_{70}Au_{70}$	—	—	—	−0.02	0.05	−0.05	−0.02		0.02	—
$Pt_{151}Au_{50}$	−0.09	−0.07	−0.08	−0.02	0.02	−0.05	−0.03	—	—	—
$Pt_{101}Au_{100}$	—	—	−0.09	−0.04	0.03	−0.05	−0.03	0.01	0.02	—
$Pt_{51}Au_{150}$	—	—	—	—	0.01	−0.06	−0.03	−0.01	0.01	0.06
$Pt_{70}Ag_{70}$				−0.17	−0.04	0.05	0.10		0.10	—
$Pt_{151}Ag_{50}$	−0.13	−0.13	−0.24	−0.11	0.02	0.12	0.15	—	—	—
$Pt_{101}Ag_{100}$	—	—	−0.30	−0.16	−0.05	0.05	0.08	0.13	0.09	—
$Pt_{51}Ag_{150}$	—	—	—	—	−0.11	−0.02	0.01	0.04	0.04	0.12
$Pt_{70}Cu_{70}$	—	−0.25		−0.23	−0.33	0.18	0.27		—	0.30
$Pt_{151}Cu_{50}$	−0.14	−0.11	−0.08	−0.07	−0.23	—	—	—	—	0.37
$Pt_{101}Cu_{100}$	—	−0.29	−0.12	−0.27	−0.39	0.27	0.22	—	0.32	0.31
$Pt_{51}Cu_{150}$	—	—	−0.57	−0.46	−0.60	0.11	0.15	—	0.19	0.19
Pt_{201}	−0.09	−0.06	−0.03	−0.01	0.07					
Au_{201}						−0.07	−0.04	−0.02	−0.01	0.04
Ag_{201}						−0.04	−0.03	0.01	−0.01	0.03
Cu_{201}						−0.05	−0.02	0.02	−0.01	0.03

$Pt_{151}Ag_{50}$, as in the $Pt_{101}Ag_{100}$ NP, result in completing the Ag skin in the former case and depleting the skin (mainly by the facet atoms) in the latter case. Comparing equilibrium chemical orderings of the 201-atomic Pt–Ag NPs with their Pt–Au analogs, see Table 2, one notices very close similarities, especially at low Pt concentrations. Indeed, topologies of most corresponding Pt–Ag and Pt–Au pairs of NPs differ at most by just small amount of heterometallic bonds contributing up to a fraction of an eV to the NP energy. It is worth mentioning that a peculiar layered chemical ordering $L1_1$ was experimentally identified inside monolayer Ag skins of some relatively small Pt–Ag NPs.[49] Small energetic preference calculated by DFT of such layering in Pt–Ag NPs[18] becomes even smaller in the analogous Pd–Ag NPs and disappears in Pt–Au and Pd–Au NPs that feature monolayer Au skins.[50] Thus, the elusive phenomenon of Pt and Pd layering inside the coinage metal skins appears to be uncommon.

$Pt_{70}Ag_{70}$ nanoparticle. Data in Tables 1 and 2 show that the size decrease of Pt–Ag NPs from 201 to 140 atoms does not change the chemical ordering pattern. In particular, the term $\varepsilon_{BOND}^{Pt\text{-}Ag} = 11^{+10}_{-13}$ meV for $Pt_{70}Ag_{70}$ NP remains within the error bar the same as for $Pt_{101}Ag_{100}$ NP, 16^{+9}_{-10} meV. Furthermore, similarly to 201-atom Pt–Ag particles, Ag atoms in $Pt_{70}Ag_{70}$ NP feature a strong stabilization in surface sites that decreases with increasing their coordination numbers, from 625 meV in the 6-coordinated corner site, to 336 meV in the 7-coordinated edge site and to 195 meV in the 9-coordinated facet (terrace) site, see Table 1. The equilibrium ordering in $Pt_{70}Ag_{70}$ NP, see Fig. 1 and Table 2, reflects these individual topological energy contributions, which lead all Ag atoms on the surface of the NP where they form a part of its monolayer skin. Ag atoms occupy all 24 edge and 24 corner positions and 22 of 48 surface terrace sites, preferring compact locations to completely occupy some of the terraces to minimize the number of Pt–Ag bonds. All 44 positions in the particle core are occupied by Pt atoms. Interestingly, the equilibrium topology of the $Pt_{70}Ag_{70}$ NP is exactly the same as that of the $Pt_{70}Au_{70}$ NP, reflecting a very similar alloying of Ag and Au atoms with Pt atoms.

Charge distribution. At variance with Pt–Au NPs, where Pt and Au atoms are basically neutral according to their Bader charges (see Section 3.1), notable electron density transfer occurs from Ag atoms to more electronegative Pt atoms in Pt–Ag NPs, see Table 3. There, surface Pt atoms acquire a negative charge reaching *ca.* −0.2 |*e*| for atoms with CN = 9 and −0.3 |*e*| for more open CN = 8 atoms. Concomitantly, surface Ag atoms bear positive charges up to 0.15 |*e*|. These data suggest noticeably different reactivity of surface Pt sites on Pt–Ag NPs compared to the corresponding sites on pure Pt NPs. Reactivity of the positively charged Ag surface sites on Pt–Ag NPs should also differ from reactivity of these sites on Ag NPs.

3.3. DFT data for chemical orderings of Pt–Cu nanoparticles

$Pt_{51}Cu_{150}$, $Pt_{101}Cu_{100}$, and $Pt_{151}Cu_{50}$ nanoparticles. Structural and electronic properties of Pt–Cu NPs are substantially different from those of the addressed above Pt–Au and Pt–Ag NPs. The energy terms ε in Table 1 reveal that Cu atoms being smaller than Pt ones (and Au and Ag atoms) are destabilized in the surface positions of Pt–Cu NPs. This occurs despite the smaller surface energy of Cu metal (0.77 eV per atom) than that of Pt metal (1.03 eV per atom).[37] Thus, relative size of the constituting atoms can reverse direction of their surface segregation in structurally stressed bimetallic nanoalloys with respect to the direction defined by the surface energies.[51] Consequently, Pt–Cu NPs at equilibrium tend to expose monolayer skins formed of Pt atoms, unlike Pt–Au and Pt–Ag NPs, which feature coinage-atom skins and Pt atoms inside the particles, see Sections 3.1 and 3.2. More specifically, based on the energies ε, 201-atom Pt–Cu NPs at different Pt:Cu compositions are more destabilized by Cu atoms in terrace positions, followed by edge and corner Cu atoms. The equilibrium orderings of $Pt_{101}Cu_{100}$ and $Pt_{51}Cu_{150}$ NPs containing surface Cu atoms first feature them in corner sites and then, at growing Cu content, in edge sites, see Table 2. An important difference of Pt–Cu NPs from Pt–Au and Pt–Ag ones is that Pt and Cu atoms favourably mix forming Pt–Cu bonds, as shown by the negative

terms $\varepsilon_{BOND}^{Pt\text{-}Cu}$, see Table 1. The mixing notably decreases the propensity to separate of two metal components in the Pt–Cu systems compared to the Pt–Au and Pt–Ag analogues, see Table 2 and Fig. 1, 2.

At the lowest studied Cu content (3 : 1 Pt : Cu), all 50 Cu atoms of $Pt_{151}Cu_{50}$ NP are energetically driven to be located inside the monolayer Pt skin and to form 412 bonds with inner and surface Pt atoms, see Table 2 and Fig. 2. At the 1 : 1 Cu : Pt content, 60 out of the 100 Cu atoms of $Pt_{101}Cu_{100}$ NP stay in the core, 24 Cu atoms occupy all corner positions and the remaining 16 Cu atoms are distributed over edge (8 atoms) and facet (8 atoms) positions. The number of Pt–Cu bonds increases to 560. At the lower 1 : 3 Pt : Cu content, all corner and edge positions of $Pt_{51}Cu_{150}$ NP are occupied by Cu atoms. Cu atoms are also located in 18 of 62 facet positions and form most of the 79-atom core. Interestingly, see Fig. 2, most of surface Pt atoms are directly neighboring other Pt atoms instead of being completely surrounded by Cu atoms, which would enable maximizing the number of Pt–Cu bonds. This implies that low Pt contents are required to form stable single Pt atoms on the surface of Pt–Cu NPs.

$Pt_{70}Cu_{70}$ nanoparticle. Similar to that atomic immiscibility of two metals in 1 : 1 201-atom Pt–Au and Pt–Ag NPs only slightly changed *vs* that in 140-atom NPs, one notices essentially the same mixing propensity of Pt and Cu atoms in $Pt_{101}Cu_{100}$ and $Pt_{70}Cu_{70}$ NPs, with $\varepsilon_{BOND}^{Pt\text{-}Cu}$ equals to −31 and −39 meV, respectively. However, the unfavorable by 15 meV corner position for Cu atom in $Pt_{101}Cu_{100}$ NP becomes favorable by 27 meV in the smaller $Pt_{70}Cu_{70}$ NP, see Table 1. The destabilizing contributions of the edge and facet positions occupied by Cu atoms remain almost the same in the 201- and 140-atomic Pt–Cu NPs. The terms ε rationalize that 100% of the corner positions and 50% of the edge positions in the lowest-energy homotop of $Pt_{70}Cu_{70}$ NP are occupied by Cu, whereas no Cu atoms are located in terrace positions and 77% of the core sites are occupied by Cu. Importantly, more than a half of all metal–metal bonds in $Pt_{70}Cu_{70}$ NP are stabilizing heterometallic Pt–Cu bonds, in comparison with only less than one-third of Pt–Au and Pt–Ag bonds in the corresponding equilibrium structures of $Pt_{70}Au_{70}$ and $Pt_{70}Ag_{70}$ NPs.

Charge distribution. Of all studied Pt nanoalloys with coinage metal, the combination Pt–Cu exhibits the highest electron density accumulated on Pt atoms, see Bader charges in Table 3, reaching up to *ca.* −0.6 $|e|$ per Pt atom depending on the NP size and Pt content. The reactivity of such strongly negatively charged surface Pt atoms is expected to significantly differ from that of Pt atoms bound to more electronegative Au, Ag, and Pt atoms. For instance, according to our calculations on-top adsorption of CO molecule on terrace Pt atoms of 201-atomic Pt–Cu NPs is *ca.* 0.2 eV weaker than of the Pt_{201} NP, in line with the propensity of more negatively charged Pt atoms in particles to bind CO adsorbate weaker.[52,53] Weakening the adsorption by merely 0.2 eV was shown to be enough for reducing CO poisoning of metal catalysts so much that their CO oxidation activity increased dramatically.[54] The reactivity of surface Cu atoms positively charged by 0.2–0.3 $|e|$ should also be singular compared with the reactivity of metallic Cu atoms, with a decreased propensity to form bonds with electrophilic species such as O. Notably, large negative charges on Pt atoms and positive charges on Cu atoms acquired upon alloying increase the size mismatch between larger Pt atoms and smaller Cu atoms. As a consequence, atoms become more displaced from their regular lattice positions in Pt–Cu NPs further affecting the reactivity of their surface sites.

3.4. Miscibility of Pt atoms with Au, Ag, and Cu atoms at the nanoscale

As already mentioned, Pt atoms in bulk alloys are immiscible at common conditions with Au and Ag atoms, but they mix with Cu atoms. These miscibility relations in the bulk are properly reflected in the terms $\varepsilon_{BOND}^{Pt\text{-}X}$ of the studied Pt–X NPs, see Table 1, manifesting relative energies of heterometallic bonds Pt–X. The energies $\varepsilon_{BOND}^{Pt\text{-}X}$ are positive for Pt–Au and Pt–Ag NPs (unfavorable formation of the heterometallic bonds) and negative for Pt–Cu NPs (favorable formation of the Pt–Cu bonds). At the nanoscale, the bulk immiscibility of bimetallic alloys can be counterbalanced by significant propensity of one metal component to segregate on the surface. That is why the equilibrium chemical orderings of Pt–Au and Pt–Ag NPs do not feature separate, as compact as possible domains of the two metals, *e.g.* Janus-type ones,[1,16] but feature core–shell arrangements with full or partially incomplete Au and Ag skins, see Fig. 1 and 2.

The miscibility of metals M and M′ in a bimetallic $M_mM'_n$ NP can be also evaluated by its excess energy *vs* the energies of the corresponding monometallic M_{n+m} and M'_{n+m} particles of the same size and structure.[7,55] The excess energy (also known as mixing energy) per atom for a Pt_mX_n particle is calculated as:

$$E_{exc}(Pt_mX_n) = \{E(Pt_mX_n) - [m/(m+n)]E(Pt_{m+n}) - [n/(m+n)]E(X_{m+n})\}/(m+n), \quad (2)$$

where a negative sign of E_{exc} indicates favorable mixing of Pt and X atoms in the particle.

The DFT excess energies of 201-atom Pt–X NPs are plotted in Fig. 3. The energies for Pt–Au and Pt–Ag NPs with Pt and X atoms that are immiscible in the bulk are spread depending on the concentrations of atoms X from −38 to −65 meV and from −58 to −90 meV, respectively. The corresponding energies for Pt–Cu NPs ranging from −127 to −163 meV are notably more negative, as expected for the miscible Pt and Cu atoms. For all these 201-atomic Pt–X NPs the miscibility in terms of the excess energies reaches maximum close to the 1 : 1 compositions. This mixing indicator remains nearly the same for the 1 : 1 140-atomic NPs, see Fig. 3: −54, −80, and −165 meV for $Pt_{70}Au_{70}$, $Pt_{70}Ag_{70}$, and $Pt_{70}Cu_{70}$, respectively.

3.5. Comparison of Pt–X and Pd–X nanoparticles (X = Au, Ag, Cu)

To better understand differences and similarities in the catalytic behavior of Pt- and Pd-based nanomaterials we compare the chemical ordering and related properties of the $Pt_{70}X_{70}$ NPs with the previously calculated data for the $Pd_{70}X_{70}$ NPs.[14]

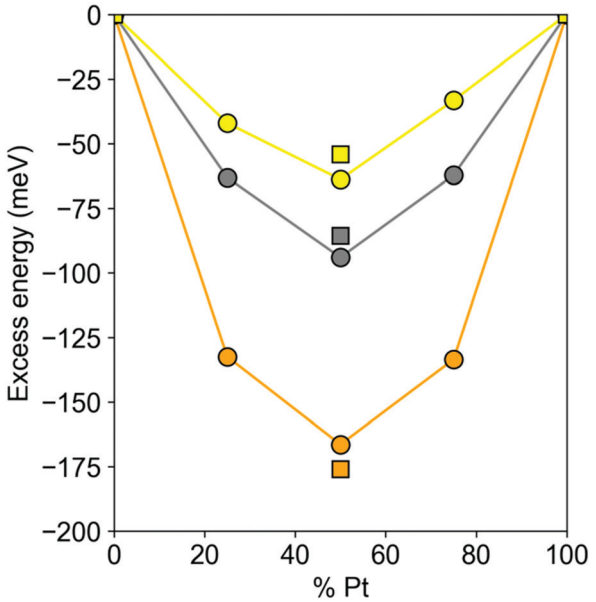

Fig. 3 DFT excess energies E_{exc} per atom (see eqn (2)) circles – of $Pt_{201-n}X_n$ (X = Au, Ag, Cu; n = 50, 100, 150) nanoparticles and squares – of $Pt_{70}X_{70}$ nanoparticles. Pt–Au – yellow, Pt–Ag – gray, Pt–Cu – orange.

The main qualitative difference of changing Pt to Pd in the nanoalloys with Au and Ag, see Table 1, is that, at variance with Pt, Pd becomes slightly miscible with these coinage metals, by −13 and −1 meV per Pd–X bond, respectively. On the other hand, the notable preference of Au and Ag atoms to occupy surface positions remains present in the Pd-based NPs, although the corresponding energies ε for them are significantly smaller than for the analogous Pt-based NPs. The stabilizing effect of the location of Au and Ag atoms in surface positions decreases in both Pt- and Pd-based NPs with increasing coordination number of the surface position. The most favorable are 6-coordinated corner sites, then 7-coordinated edge sites, and finally 9-coordinated sites in the {111} facets. Similarities of the energies ε for the corresponding $Pt_{70}X_{70}$ and $Pd_{70}X_{70}$ (X = Ag, Au) NPs result in similar orderings of their lowest-energy homotops. In all four NPs X atoms occupy all 48 corner plus edge sites, while the remaining 22 X atoms are located in the {111} facet sites. Pt and Pd atoms occupy the remaining 26 surface sites of the facets and all 44 positions in the interior of the NPs. The main difference in the orderings comes from the number of heterometallic bonds. The equilibrium $Pt_{70}X_{70}$ structures feature 196 Pt–X bonds, 31% of overall 636 bonds in the 140-atomic NP, to be compared with significantly larger number of heterometallic bonds in the $Pd_{70}X_{70}$ structures, 234–262 (37–41%). A consequence of the different numbers of the heterometallic bonds is that most of the {111} facets in the $Pt_{70}X_{70}$ structures are formed by either only X or only Pt atoms, whereas the individual facets in the $Pd_{70}X_{70}$ structures contain a mixture of X and Pd atoms, increasing the number of Pd–X bonds.

Miscibility of the coinage and platinum-group metal atoms is favorable in both $Pt_{70}Cu_{70}$ and $Pd_{70}Cu_{70}$ NPs, see Table 1. Each heterometallic bond stabilizes the former particle by 9 meV more than the latter. The occupation of surface positions by Cu destabilizes these two NPs, with one exception. Namely, the occupation of corner position of $Pt_{70}Cu_{70}$ NP by atom Cu instead of atom Pt has a slight stabilizing effect, by −27 meV. The destabilization due to the presence of surface Cu atoms increases with increasing their coordination numbers, though the destabilization values (energy differences between the most stable and the least stable surface positions) are quite different, 371 meV for $Pt_{70}Cu_{70}$ and 88 meV for $Pd_{70}Cu_{70}$. It is least favorable for Cu atoms to occupy terrace sites of $Pt_{70}Cu_{70}$ and $Pd_{70}Cu_{70}$ NPs. Cu atoms are differently distributed on the surface of $Pt_{70}Cu_{70}$ and $Pd_{70}Cu_{70}$ homotops with the lowest E^{TOP} energy. In the $Pt_{70}Cu_{70}$ NP, 36 surface Cu atoms occupy all 24 corner positions and a half of 24 edge positions, leaving all 48 terrace positions to be occupied by Pt atoms, see Table 2. 32 surface Cu atoms of the $Pd_{70}Cu_{70}$ NP are quite evenly spread over three types of sites: corner – 12, edge – 14, and terrace – 8[14] as a result of relatively small energy difference of Cu in these sites. To maximize the number of stabilizing heterometallic bonds the equilibrium $Pt_{70}Cu_{70}$ and $Pd_{70}Cu_{70}$ structures are of quite common onion-like type,[1,2,56,57] with Pt/Pd-rich core, Cu-rich subsurface shell and monatomic skin shared by Pt/Pd and Cu atoms. These chemical orderings allow formation of 340 Pt–Cu and 382 Pd–Cu bonds.

The present topological approach has been recently employed to analyze in detail the formation of single-atom Pd sites in Pd–Au NPs appealing for catalysis as a function of Pd concentration inside the particles.[17] It was shown that no surface Pd atoms emerge at low Pd concentrations in the Au skin at equilibrium chemical orderings. Single-atom surface Pd sites become stable in 201-atom Pd–Au particles when Pd content inside the skin reaches *ca.* 60% (corresponding to 153 Au and 48 Pd atoms) and further increase of Pd content results in more surface Pd, first mostly as single atoms. Such emergence of surface Pd atoms is triggered by stabilizing Pd–Au bonds reflected in negative $\varepsilon_{BOND}^{Pd\text{-}Au}$ energies for Pd–Au NPs.[13–15,17] According to $\varepsilon_{BOND}^{Pt\text{-}X}$ (Table 1), heterometallic bonds of Pt are stabilizing neither in Pt–Au, nor in Pt–Ag NPs. Thus, the location of Pt atoms is not favored on the surface of Pt–Au and Pt–Ag NPs at the equilibrium orderings, unless the number of Au and Ag atoms in these particles is smaller than the 122 required to form complete coinage-metal skins. However, single-atom Pt sites can be easily created on the surface of Pt–Au and Pt–Ag NPs in the course of catalytic reactions already at low Pt concentration due to energetically preferable interactions of Pt centers with reactants and intermediates compared to Au and Ag centers. This adsorbate-induced surface segregation phenomenon is well known for nanoalloy catalysts.[13,16,21,23,25,26,51] In the cases of Pd–Cu and Pt–Cu NPs Pd and Pt atoms show a strong preference to be located in the surface skin and to form stabilizing heterometallic bonds, see Tables 1 and 2. Thus, the presence of Pd and Pt on the surface of these nanoalloys as unique single-atom catalytic sites is conceivable only at very low concentration of the platinum-group metals.

3.6. Performance of the topological method to describe chemical orderings

The present TOP method[14,15] focuses on patterns of the equilibrium chemical orderings of bimetallic NPs, which determine the surface reactivity. The method employs a very simple topological equation (*i.e.* in the form of eqn (1)) to pre-screen a huge number of the chemical orderings (homotops) of a NP to find several best candidates in terms of their lowest E^{TOP} energies for subsequent electronic-structure (DFT) calculations with locally relaxed positions of atoms. Among the method simplifications are: (i) accounting only for interactions between nearest-neighbor pairs of atoms and assuming all bond of the same type (*e.g.* all Pt–Pt bonds) to be equal; (ii) describing positions of atoms in the NP lattice solely by the coordination numbers, distinguishing between surface atoms with different coordination numbers but treating all atoms of each metal type inside the NP as equivalent; (iii) grouping homotops in so-called topologies of the same $N_{BOND}^{Pt-X} \cdot N_{CORNER}^{X} \cdot N_{EDGE}^{X} \cdot N_{FACET}^{X}$ numbers in eqn (1), and assuming that an arbitrarily chosen homotop of a given topology represents reasonably well the DFT energy and the chemical ordering of all other numerous homotops of the same topology.

To evaluate the correctness of some of these assumptions we randomly generated $\geq$10 different homotops for several selected topologies of Pt–Au and Pt–Cu NPs and locally optimized those by DFT; see results in Table S1 (ESI†). The DFT energy splits for the homotops belonging to each of the considered low-energy topologies of 201-atomic Pt–Au NPs are very small, up to *ca.* 1 meV per atom. The splits slightly increase with growing content of Au atoms (preferably located on the surface), ranging from only 25 meV for the topology $Pt_{151}Au_{50}$_214.20.30.0 to 286 meV for the topology $Pt_{51}Au_{150}$_210.24.36.62. DFT energy splits for low-lying topologies of Pt–Cu NPs noticeably increased compared to the corresponding Pt–Au NPs. Noteworthy, the Pt–Cu energy splits also increase with growing content of Pt on the surface, from 153 meV for the topology $Pt_{51}Cu_{150}$_418.24.36.18 to 930 meV for the topology $Pt_{151}Cu_{50}$_412.0.0.0, the latter with solely Pt atoms on the surface. We note that the prediction error of E^{TOP} *vs.* E^{DFT} energies for such low-energy orderings range from 1.1 to 6.8 meV per atom (see Table S1, ESI†), although the errors for high-energy structures are significantly larger. For many practical applications, the up to *ca.* 7 meV per atom uncertainty in total energy of the $Pt_{151}Cu_{50}$_412.0.0.0 homotops provided by the present computational setup may be sufficient. If not, DFT calculations can be performed, as just discussed, for additional homotops of the putative lowest-energy topologies, to more precisely approach equilibrium DFT chemical orderings.

A similar procedure could be applied to go beyond the topology approach, when a more precise energetic representation of chemical orderings is required for assessing notably higher-lying homotops. One can see from Table S1 (ESI†) a substantial energy split in one of the higher-lying topologies of 201-atomic NPs, namely by 1501 meV in $Pt_{101}Au_{100}$_594.24.0.54, but this seems to be not very often the case.

Interestingly, the energy splitting for 10 random homotops with putative lowest-energy topologies $Pt_{70}Au_{70}$_196.24.24.22 and $Pt_{70}Cu_{70}$_340.24.12.0, 1027 and 1568 meV, respectively, see structures of the homotops with minimum and maximum DFT energies of these topologies in Fig. S1 (ESI†), are notably larger than those for the 201-atom Pt–Au and Pt–Cu NPs. Again, the Pt–Cu homotops split more than the Pt–Au homotops. Our detailed analysis of this splitting reveals that not all atoms of one type (Pt–Pt, Pt–X, or X–X bonds) are equivalent, *i.e.* that the energy of bonds formed by Pt or X atoms to each of their first neighbours is partially dependent on the identity (and quantity) of the rest of first neighbours. This challenges the convenient assumption that all bonds between a given pair of atoms are equally strong. In addition, certain structural motifs (such as {111} facets solely composed of Au) seem to become stable for some compositions due to elusive long-range interactions neglected by the employed topological description.

Although the δ values in Table 1 may seem large, they correspond to average prediction errors 1 to 6 meV per atom. The large size of the studied particles obviously increases the errors in total energies, but changes in energy caused by permuting atoms are, on average, rather well approximated. This means that irrespective of possible inaccuracies of the present TOP approach based on the DFT structure optimization, the equilibrium chemical orderings in bimetallic nanoalloys provided by this approach approximate reasonably well those obtained with the employed DFT exchange–correlation functional. The calculated atomic-level data, which are notably more detailed than those currently accessible experimentally, are very useful for rationalizing surface reactivity of bimetallic catalysts and related applications.

3.7. Larger Pt-based nanoparticles and temperature effects on the chemical ordering

Chemical orderings with the lowest-energy topology were also determined for *ca.* 4.4 nm large fcc truncated octahedral $Pt_{732}X_{731}$ NPs using the energies ε obtained for 140-atomic $Pt_{70}X_{70}$ and for 201-atomic $Pt_{101}X_{100}$ NPs, see Table 1. Orderings of these homotops at 0 K, denoted as $Pt_{732}X_{731}^{(140)}$ and $Pt_{732}X_{731}^{(201)}$, respectively, are shown in Fig. 4 and occupations of various atomic positions in them are quantified in Table 4. As the 1463-atomic particles are too large for DFT calculations, results for them were obtained only using the Monte Carlo simulation part of the Topological description approach,[14,15] *vide supra*.

Usage of both the (140) and (201) sets of energies ε results in the same topologies of the lowest-energy orderings of $Pt_{732}Au_{731}$ and $Pt_{732}Ag_{731}$ NPs. These are core–shell orderings with Au and Ag atoms occupying all surface and a part of subsurface positions, while Pt atoms form compact cores inside the monolayer skins of coinage metals. Since Au and Ag atoms tend to surface segregate and Pt–Au and Pt–Ag bonds are destabilizing with respect to forming homometallic bonds, by 11–21 meV each, these 1238 bonds comprise only 16% of all 7776 bonds in the 1463-atom NPs, see Table 4.

The equilibrium ordering in $Pt_{732}Cu_{731}$ NP is more complex, reflecting that Pt–Cu bonds are stabilizing with respect to the corresponding homometallic bonds, and that smaller Cu atoms

alloyed with Pt are less disfavored when located inside the particles compared to Au and Ag atoms. In $Pt_{732}Cu_{731}^{(140)}$ all 24 corner positions are occupied by Cu atoms, each of them stabilizing the system by −27 meV with respect to having Pt in the same positions. Occupation of almost a half of edge positions by Cu atoms alternating with Pt atoms to increase the number of favorable Pt–Cu bonds partially counterbalanced the preference, by 181 meV, of each edge Pt atom compared to having an edge Cu atom. A layered arrangement of inner Pt and Cu atoms seems to be also result from an increased number of favorable Pt–Cu bonds. No Cu atoms occupy terrace sites in line with the largest destabilization by 344 meV per terrace Cu atom with respect to having a Pt atom in those positions. Interestingly, the number of surface Cu atoms in the $Pt_{732}Cu_{731}^{(201)}$ NP, 167, is more than twice larger than in the $Pt_{732}Cu_{731}^{(140)}$ NP, 72. This finding seems counterintuitive based on the energies ε, which indicate stronger destabilization of surface Cu atoms in $Pt_{101}Cu_{100}$ NP than in $Pt_{70}Cu_{70}$ NP. It can be explained by the fact that Cu atoms in the $Pt_{732}Cu_{731}^{(201)}$ NP are scattered and mostly surrounded by Pt atoms forming more favorable Pt–Cu contacts. Indeed, there are more Pt–Cu bonds in the structure $Pt_{732}Cu_{731}^{(201)}$, 4543 (58%), than in $Pt_{732}Cu_{731}^{(140)}$, 3868 (50%), since the $\varepsilon_{BOND}^{Pt\text{-}Cu}$ values for the 201- and 140-atomic NPs are −43 and −35 meV, respectively. The energy gain due to an increased number of Pt–Cu contacts in $Pt_{732}Cu_{731}^{(201)}$ NP, −29.025 eV according to the energies ε, see Table 1, overcompensates the energy penalty caused by the presence of more surface Cu atoms, 26.429 eV. Thus, the equilibrium ordering $Pt_{732}Cu_{731}^{(201)}$ is estimated to be *ca.* 2.6 eV more stable than $Pt_{732}Cu_{731}^{(140)}$ one, which for such large particles translates in a difference of 1.8 meV per atom. Note that many adsorbates from the reacting media interact with Pt surface sites at least

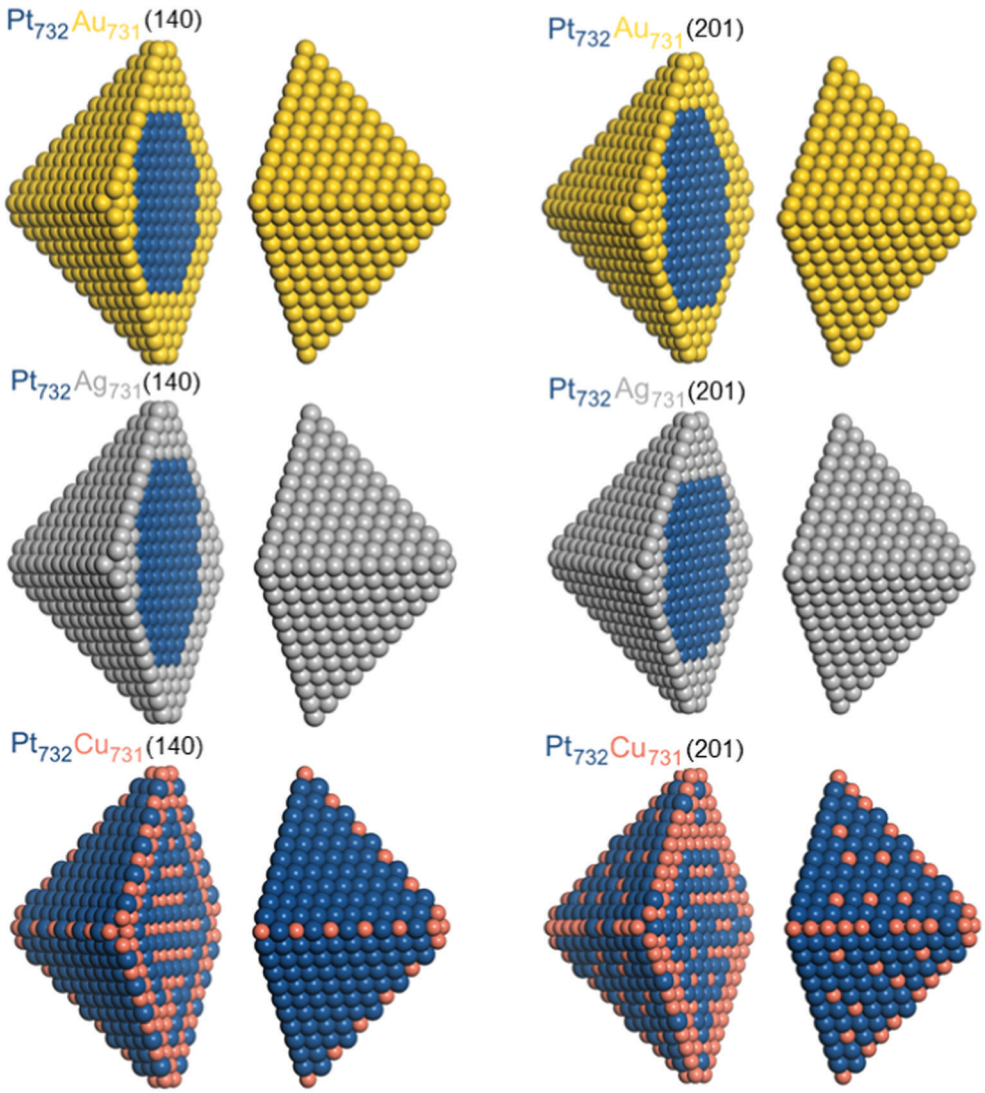

Fig. 4 Equilibrium chemical orderings of *ca.* 4.4 nm large truncated-octahedral fcc $Pt_{732}Au_{731}$, $Pt_{732}Ag_{731}$, and $Pt_{732}Cu_{731}$ nanoparticles at 0 K with the lowest TOP energies calculated using eqn (1) for $Pt_{70}X_{70}$ particles ($Pt_{732}X_{731}^{(140)}$, left column) and $Pt_{101}X_{100}$ (particles $Pt_{732}X_{731}^{(201)}$, right column). Colors of atoms are as in Fig. 1.

Table 4 Chemical ordering in the representative lowest-energy $Pt_{732}X_{731}^{(140)}$ and $Pt_{732}X_{731}^{(201)}$ homotops at different temperature calculated using the TOP equations (see Table 1) for the $Pt_{70}X_{70}$ and $Pt_{101}X_{100}$ NPs, respectively. In parentheses are the fractions (in %) of the total numbers of the metal–metal bonds or atoms X in various lattice positions of $Pt_{732}X_{731}$ NPs

Nanoparticle	T, K	$N_{BOND}^{Pt\text{-}X}$	N_{CORNER}^{X}	N_{EDGE}^{X}	N_{FACET}^{X}	N_{INSIDE}^{X}
$Pt_{732}Au_{731}^{(140)}$	0	1238 (16)	24 (100)	108 (100)	440 (100)	159 (18)
$Pt_{732}Au_{731}^{(201)}$	0	1238 (16)	24 (100)	108 (100)	440 (100)	159 (18)
	300	1309 (17)	24 (100)	108 (100)	439 (100)	160 (18)
	600	1502 (19)	24 (100)	107 (99)	439 (100)	161 (18)
	1000	1885 (24)	23 (96)	108 (100)	433 (98)	167 (19)
$Pt_{732}Ag_{731}^{(140)}$	0	1238 (16)	24 (100)	108 (100)	440 (100)	159 (18)
$Pt_{732}Ag_{731}^{(201)}$	0	1238 (16)	24 (100)	108 (100)	440 (100)	159 (18)
	300	1354 (17)	24 (100)	108 (100)	440 (100)	159 (18)
	600	1671 (21)	24 (100)	107 (99)	440 (100)	160 (18)
	1000	2129 (27)	24 (100)	108 (100)	429 (98)	170 (19)
$Pt_{732}Cu_{731}^{(140)}$	0	3868 (50)	24 (100)	48 (44)	0 (0)	659 (74)
$Pt_{732}Cu_{731}^{(201)}$	0	4543 (58)	24 (100)	86 (80)	57 (13)	564 (63)
	300	4343 (56)	23 (96)	63 (58)	58 (13)	587 (66)
	600	4244 (55)	21 (88)	61 (56)	73 (17)	576 (65)
	1000	4183 (54)	19 (79)	55 (51)	98 (22)	559 (63)

The total topological numbers for the $Pt_{732}X_{731}$ particles are: N_{BOND} = 7776, N_{CORNER} = 24, N_{EDGE} = 108, N_{FACET} = 440, N_{INSIDE} = 891.

1 eV stronger than with the corresponding Cu sites. Therefore, similar changes of the ordering patterns as those simulated for the structures $Pt_{732}Cu_{731}^{(201)}$ and $Pt_{732}Cu_{731}^{(140)}$, see Fig. 4, can be easily caused at experimental conditions in Pt–Cu NPs by adsorbing even a few reacting species from the environment.

The calculated results presented so far have corresponded to equilibrium structurers at temperature 0 K. Since the TOP method allows to approximately account for entropy effects associated with the chemical orderings (neglecting vibrational contributions), we employed a computational setup introduced elsewhere[15] for estimating properties associated with Boltzmann population of different homotops. Specifically, we calculated the average topology in the $Pt_{732}X_{731}$ (X = Au, Ag, Cu) NPs in the temperature range 0–1000 K by means of the Metropolis Monte Carlo algorithm. In particular, the averaging was done over accepted configurations obtained during an MC run at a given temperature, which results in the probability of occupying of each site by either Pt or X atoms. The homotop with the most similar topology to the calculated average is then chosen as the representative model for each run. As expected, temperature increase noticeably increased the disorder in all modeled particles, see Table 4 and Fig. 5 for the results corresponding to 300, 600, and 1000 K.

For instance, several Pt atoms appeared at 600 and 1000 K on the surface of $Pt_{732}Au_{731}$ and $Pt_{732}Ag_{731}$ NPs that exhibited complete surface shells of Au and Ag atoms at 0 and 300 K. Concomitantly, single Au and Ag atoms migrated in the compact Pt cores. Also, the number of both Pt–Au and Pt–Ag bonds

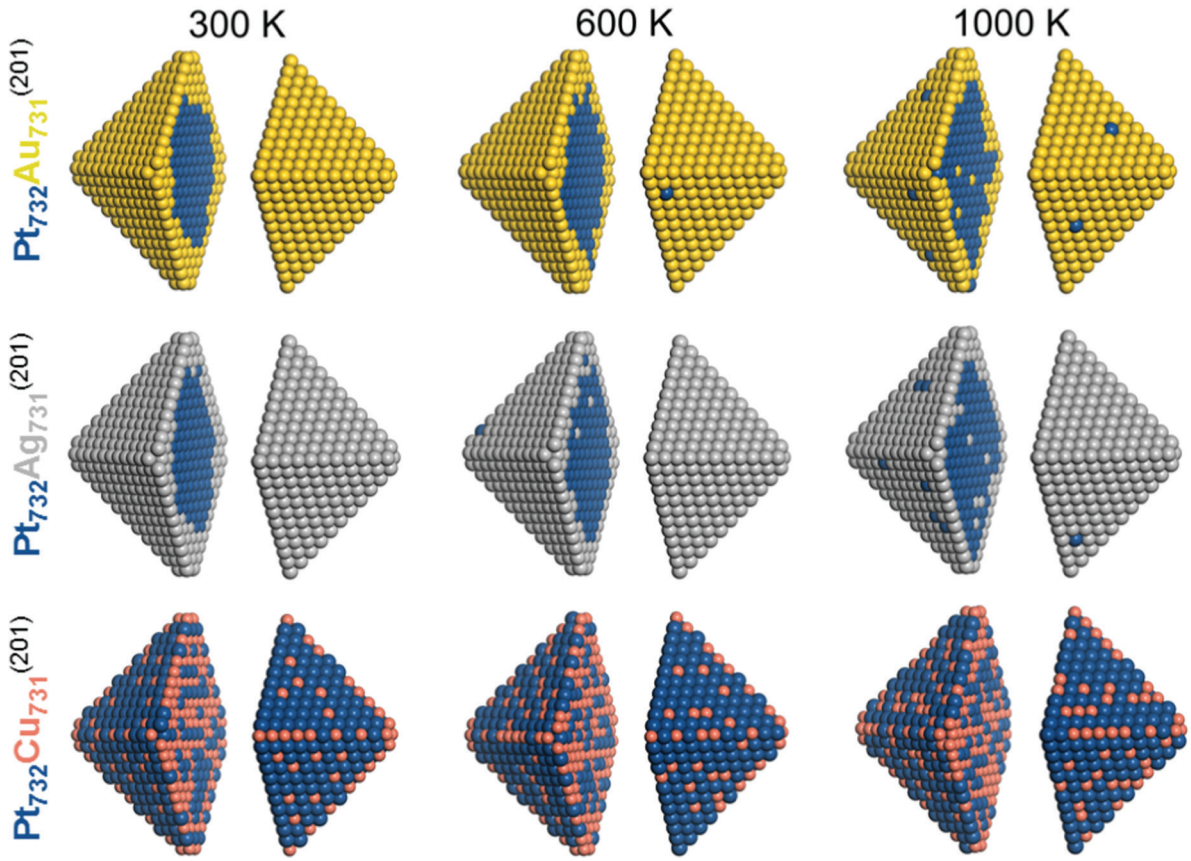

Fig. 5 Equilibrium chemical orderings of $Pt_{732}Au_{731}$, $Pt_{732}Ag_{731}$, and $Pt_{732}Cu_{731}$ nanoparticles at temperatures 300 K, 600 K and 1000 K calculated using eqn (1) for the corresponding $Pt_{101}Au_{100}$, $Pt_{101}Ag_{100}$, and $Pt_{101}Cu_{100}$ particles. Colors of atoms are as in Fig. 1.

increased with the temperature increase. The fraction of Pt–Au bonds in $Pt_{732}Au_{731}$ NP increased from 16% (0 K) to 17% (300 K), 19% (600 K), and 24% (1000 K). The corresponding number of bonds in $Pt_{732}Ag_{731}$ NP increases somewhat more steep at elevated temperature, in line with less destabilizing character of Pt–Ag bonds compared with Pt–Au bonds.

In $Pt_{732}Cu_{731}$ NP the number of stabilizing Pt–Cu bonds slightly decreased at higher temperatures, from 58% at 0 K to 54% at 1000 K. Cu atoms migrate upon the temperature increase from corner and edge positions most populated at 0 K primarily to surface terrace positions.

4. Summary and conclusions

We determined equilibrium chemical orderings in truncated-octahedral Pt–Au, Pt–Ag, and Pt–Cu nanoparticles containing 140 and 201 atoms at metals concentrations 3 : 1, 1 : 1, and 1 : 3 by means of DFT calculations combined with the Topological approach.[14,15]

The equilibrium chemical orderings in the Pt–Au and Pt–Ag particles with $\leq$201 atoms closely resemble each other: Au and Ag atoms are strongly energetically driven to be on the surface, whereas Pt atoms preferentially occupy inner positions. The immiscibility of Au and Ag atoms with Pt atoms prevents the appearance of Pt atoms on the surface of these nanoalloys as single-atom catalytic sites until the coinage metal content becomes low. Atoms in Pt–Au nanoparticles are essentially neutral, whereas in Pt–Ag nanoparticles Pt and Ag atoms are moderately charged negatively and positively, respectively. This suggests noticeably different reactivity of surface Pt sites on Pt–Ag than on single-metal Pt particles.

In Pt–Cu nanoparticles, Pt atoms are driven to the surface and most stabilized in the 9- and 8-coordinated positions of the {111} and {100} nanofacets. Pt–Cu bonds formed upon the favorable mixing of Pt and Cu atoms induce a strong Cu to Pt charge transfer. The up to half of an electron transferred to surface Pt atoms from nearby Cu atoms is expected to substantially affect the surface reactivity of both Pt and Cu sites.

Ordering trends in Pt–X nanoalloys are quite similar to the trends in previously characterized Pd–X nanoalloys, *i.e.* with the coinage metal atoms at the surface for X = Au or Ag, and rather well mixed orderings for X = Cu. The main difference is that heterometallic bonds slightly destabilize (with respect to homometallic bonds) Pt–Ag and Pt–Au particles, but stabilize Pd–Ag and Pd–Au ones, leading to more mixed terraces in the later two.

The most stable orderings in *ca.* 4.4 nm $Pt_{732}Au_{731}$ and $Pt_{732}Ag_{731}$ particles are of the Pt–core/Au(Ag)–shell type. The lowest-energy chemical ordering pattern of $Pt_{732}Cu_{731}$ particle is characterized by surface Cu atoms scattered over Pt atoms in the facets and quite randomly distributed inner atoms of both metals. Modelling the evolution of the orderings upon temperature increase revealed that heating leads to the appearance of single-atom or diatomic surface Pt sites on facets of $Pt_{732}Au_{731}$ and $Pt_{732}Ag_{731}$ particles and increases the disorder and number of surface Cu atoms on facets of $Pt_{732}Cu_{731}$ particle. New surface sites with correspondingly different chemical properties are formed upon heating.

The results presented in this work are relevant for studies in which structure and surface properties of a large number of bimetallic compositions are simulated using machine-learning and/or high-throughput approaches. Such studies often relied on models produced by directly cutting bulk structures,[58,59] without considering that due to the stability of particular chemical orderings inherently different sites can be exposed on the surface.

Author contributions

L. Vega: calculations, conceptualization, data curation, formal analysis, investigation, methodology, validation, visualization, writing – original draft, review & editing; H. A. Aleksandrov: calculations, conceptualization, investigation, methodology, writing – original draft, review & editing; F. Viñes: investigation, supervision, validation, writing – review & editing; R. Farris: calculations, validation; A. Bruix: investigation, methodology, validation, writing – review & editing; K. M. Neyman: conceptualization, methodology, project administration, supervision, validation, writing – original draft, review & editing.

Conflicts of interest

There are no conflicts to declare.

Acknowledgements

Authors acknowledge support by the grants PGC2018-093863-B-C22, RTI2018-095460-B-I00, and MDM-2017-0767 of the Spanish Ministerio de Ciencia y Universitades as well as by the grant 2017SGR13 of the Generalitat de Catalunya. HAA is grateful to the Operational Program ''Science and Education for Smart Growth'' under contract UNITe No. BG05M2OP001-1.001-0004-C01 (2018–2023). The Generalitat de Catalunya financed the work of LV (*via* pre-doctoral grant 2018FI-B-00384) and AB (*via* grant 2018BP00190). Research contribution of RF has been supported by a visiting grant HPC17YE51L of the HPC-Europa3 program. The study was also supported by Bulgarian Ministry of Education and Science *via* the contract D01-76/2021 and by European COST Action CA18234. Computer resources have been partly provided by the Red Española de Supercomputación (projects QS-2020-2-0020, QS-2019-3-0023, QSM-2018-1-0029).

References

1 R. Ferrando, J. Jellinek and R. L. Johnston, Nanoalloys: From Theory to Applications of Alloy Clusters and Nanoparticles, *Chem. Rev.*, 2008, **108**, 845–910.
2 F. Calvo, *Nanoalloys from Fundamentals to Emergent Applications*, Elsevier, Amsterdam, 2013.

3 I. V. Yudanov, R. Sahnoun, K. M. Neyman and N. Rösch, Carbon Monoxide Adsorption on Palladium Nanoparticles: A Relativistic Density Functional Study, *J. Chem. Phys.*, 2002, **117**, 9887–9896.
4 I. V. Yudanov, R. Sahnoun, K. M. Neyman, N. Rösch, J. Hoffmann, S. Schauermann, V. Johánek, H. Unterhalt, G. Rupprechter, J. Libuda and H.-J. Freund, CO Adsorption on Pd Nanoparticles: Density Functional and Vibrational Spectroscopy Studies, *J. Phys. Chem. B*, 2003, **107**, 255–264.
5 A. Roldán, F. Viñes, F. Illas, J. M. Ricart and K. M. Neyman, Density Functional Studies of Coinage Metal Nanoparticles: Scalability of Their Properties to Bulk, *Theor. Chem. Acc.*, 2008, **120**, 565–573.
6 K. M. Neyman, R. Sahnoun, C. Inntam, S. Hengrasmee and N. Rösch, Computational Study of Model Pd–Zn Nanoclusters and Their Adsorption Complexes with CO Molecules, *J. Phys. Chem. B*, 2004, **108**, 5424–5430.
7 I. V. Yudanov and K. M. Neyman, Stabilization of Au at Edges of Bimetallic PdAu Nanocrystallites, *Phys. Chem. Chem. Phys.*, 2010, **12**, 5094–5100.
8 J. Ryosuke, K. K. T. Suzuki and Y. Morimoto, DFT Calculations on Electro-Oxidations And Dissolutions of Pt and Pt–Au Nanoparticles, *Catal. Today*, 2016, **262**, 100–109.
9 L. Piccolo, Z. Y. Li, I. Demiroglu, F. Moyon, Z. Konuspayeva, G. Berhault, P. Afanasiev, W. Lefebvre, J. Yuan and R. L. Johnston, Understanding And Controlling The Structure And Segregation Behaviour of AuRh Nanocatalysts, *Sci. Rep.*, 2016, **6**, 35226.
10 M. Hu, D. P. Linder, M. B. Nardelli and A. Striolo, Hydrogen Adsorption on Platinum–Gold Bimetallic Nanoparticles: A Density Functional Theory Study, *J. Phys. Chem. C*, 2013, **117**, 15050–15060.
11 X. Lei, H. Mu, S. Li, G. Liu, B. Xu and C. Ouyang, The Structural and Electronic Properties of Pt–Cu Alloy Clusters: Embedding Atom Method Combined with Density Functional Theory Study, *J. Alloys Compd.*, 2018, **741**, 604–609.
12 L.-L. Wang and D. D. Johnson, Predicted Trends of Core-Shell Preferences for 132 Late Transition-Metal Binary-Alloy Nanoparticles, *J. Am. Chem. Soc.*, 2009, **131**, 14023–14029.
13 M. Mamatkulov, I. V. Yudanov, A. V. Bukhtiyarov, I. P. Prosvirin, V. I. Bukhtiyarov and K. M. Neyman, Pd Segregation on the Surface of Bimetallic PdAu Nanoparticles Induced by Low Coverage of Adsorbed CO, *J. Phys. Chem. C*, 2019, **123**, 8037–8046.
14 S. M. Kozlov, G. Kovács, R. Ferrando and K. M. Neyman, How to Determine Accurate Chemical Ordering in Several Nanometer Large Bimetallic Crystallites from Electronic Structure Calculations, *Chem. Sci.*, 2015, **6**, 3868–3880.
15 G. Kovács, S. M. Kozlov and K. M. Neyman, Versatile Optimization of Chemical Ordering in Bimetallic Nanoparticles, *J. Phys. Chem. C*, 2017, **121**, 10803–10808.
16 L. Vega, H. A. Aleksandrov and K. M. Neyman, Using Density Functional Calculations to Elucidate Atomic Ordering of Pd-Rh Nanoparticles at Sizes Relevant for Catalytic Applications, *Chin. J. Catal.*, 2019, **40**, 1749–1757.
17 M. Mamatkulov, I. V. Yudanov, A. V. Bukhtiyarov and K. M. Neyman, Pd Single-atom Sites on the Surface of PdAu Nanoparticles: A DFT-based Topological Search for Suitable Compositions, *Nanomaterials*, 2021, **11**, 122.
18 S. Olobardi, L. Vega, A. Fortunelli, M. Stener, F. Viñes and K. M. Neyman, Optical Properties and Chemical Ordering of Ag–Pt Nanoalloys: A Computational Study, *J. Phys. Chem. C*, 2019, **123**, 25482–25491.
19 G. Kovács, S. M. Kozlov, I. Matolínová, M. Vorokhta, V. Matolín and K. M. Neyman, Revealing Chemical Ordering in Pt–Co Nanoparticles Using Electronic Structure Calculations and X-ray Photoelectron Spectroscopy, *Phys. Chem. Chem. Phys.*, 2015, **17**, 28298–28310.
20 M. Vorokhta, I. Khalakhan, M. Václavů, G. Kovács, S. M. Kozlov, P. Kúš, T. Skála, N. Tsud, J. Lavková, V. Potin, I. Matolínová, K. M. Neyman and V. Matolín, Surface Composition of Magnetron Sputtered Pt–Co Thin Film Catalyst for Proton Exchange Membrane Fuel Cells, *Appl. Surf. Sci.*, 2016, **365**, 245–251.
21 I. Khalakhan, L. Vega, M. Vorokhta, T. Skála, F. Viñes, Y. V. Yakovlev, K. M. Neyman and I. Matolínová, Irreversible Structural Dynamics on the Surface of Bimetallic PtNi Alloy Catalyst under Alternating Oxidizing And Reducing Environments, *Appl. Catal., B*, 2020, **264**, 118476.
22 A. Neitzel, G. Kovács, Y. Lykhach, S. M. Kozlov, N. Tsud, T. Skála, M. Vorokhta, V. Matolín, K. M. Neyman and J. Libuda, Atomic Ordering and Sn Segregation in Pt–Sn Nanoalloys Supported on CeO_2 Thin Films, *Top. Catal.*, 2017, **60**, 522–532.
23 A. Wolfbeisser, G. Kovács, S. M. Kozlov, K. Föttinger, J. Bernardi, B. Klötzer, K. M. Neyman and G. Rupprechter, Surface Composition Changes of CuNi-ZrO_2 During Methane Decomposition: An Operando NAP-XPS and Density Functional Study, *Catal. Today*, 2017, **283**, 134–143.
24 L. Liu and A. Corma, Metal Catalysts for Heterogeneous Catalysis: From Single Atoms to Nanoclusters and Nanoparticles, *Chem. Rev.*, 2018, **118**, 4981–5079.
25 L. Li, X. Chang, X. Lin, Z.-J. Zhao and J. Gong, Theoretical Insights into Single-Atom Catalysts, *Chem. Soc. Rev.*, 2020, **49**, 8156–8178.
26 R. T. Hannagan, G. Giannakakis, M. Flytzani-Stephanopoulos and E. C. H. Sykes, Single-Atom Alloy Catalysis, *Chem. Rev.*, 2020, **120**, 12044–12088.
27 G. Kresse and J. Furthmüller, Efficient Iterative Schemes for *Ab Initio* Total-Energy Calculations Using a Plane-Wave Basis Set, *Phys. Rev. B: Condens. Matter Mater. Phys.*, 1996, **54**, 11169–11186.
28 G. Kresse and J. Hafner, *Ab Initio* Molecular-Dynamics Simulation of the Liquid-Metal–Amorphous-Semiconductor Transition in Germanium, *Phys. Rev. B: Condens. Matter Mater. Phys.*, 1994, **49**, 14251–14269.
29 J. P. Perdew, K. Burke and M. Ernzerhof, Generalized Gradient Approximation Made Simple, *Phys. Rev. Lett.*, 1996, **77**, 3865–3868; J. P. Perdew, K. Burke and M. Ernzerhof, *Phys. Rev. Lett.*, 1997, **78**, 1396.
30 P. Janthon, S. M. Kozlov, F. Viñes, J. Limtrakul and F. Illas, Establishing the Accuracy of Broadly Used Density

Functionals in Describing Bulk Properties of Transition Metals, *J. Chem. Theory Comput.*, 2013, **9**, 1631–1640.
31 P. Janthon, S. Luo, S. M. Kozlov, F. Viñes, J. Limtrakul, D. G. Truhlar and F. Illas, Bulk Properties of Transition Metals: A Challenge for the Design of Universal Density Functionals, *J. Chem. Theory Comput.*, 2014, **10**, 3832–3839.
32 L. Vega, J. Ruvireta, F. Viñes and F. Illas, Jacob's Ladder as Sketched by Escher: Assessing the Performance of Broadly Used Density Functionals on Transition Metal Surface Properties, *J. Chem. Theory Comput.*, 2018, **14**, 395–403.
33 P. E. Blöchl, Projector Augmented-Wave Method, *Phys. Rev. B: Condens. Matter Mater. Phys.*, 1994, **50**, 17953–17979.
34 G. Kresse and D. Joubert, From Ultrasoft Pseudopotentials to the Projector Augmented-Wave Method, *Phys. Rev. B: Condens. Matter Mater. Phys.*, 1999, **59**, 1758–1775.
35 F. Viñes, F. Illas and K. M. Neyman, On the Mechanism of Formation of Metal Nanowires by Self-Assembly, *Angew. Chem., Int. Ed.*, 2007, **46**, 7094–7097.
36 S. M. Kozlov, H. A. Aleksandrov, J. Goniakowski and K. M. Neyman, Effect of MgO(100) Support on Structure and Properties of Pd and Pt Nanoparticles with 49–155 Atoms, *J. Chem. Phys.*, 2013, **139**, 084701.
37 A. Ruban, H. L. Skriver and J. K. Nørskov, Surface Segregation Energies in Transition-Metal Alloys, *Phys. Rev. B: Condens. Matter Mater. Phys.*, 1999, **59**, 15990–16000.
38 V. Grolier and R. Schmid-Fetzer, Experimental Study of Au–Pt–Sn Phase Equilibria and Thermodynamic Assessment of the Au–Pt and Au–Pt–Sn Systems, *J. Electron. Mater.*, 2008, **37**, 264–278.
39 L. Deng, W. Hu, H. Deng and S. Xiao, Surface Segregation and Structural Features of Bimetallic Au–Pt Nanoparticles, *J. Phys. Chem. C*, 2010, **114**, 11026–11032.
40 S. Takizawa, K. Terakura and T. Mohri, Electronic Theory for Phase Stability of Nine AB Binary Alloys, with A = Ni, Pd, or Pt and B = Cu, Ag, or Au, *Phys. Rev. B: Condens. Matter Mater. Phys.*, 1989, **39**, 5792–5797.
41 O. Kubaschewski, C. B. Alcock and P. J. Spencer, *Materials Thermochemistry*, Oxford, Pergamon, 6th edn, 1993.
42 J. Tang, L. Deng, S. Xiao, H. Deng, X. Zhang and W. Hu, Chemical Ordering and Surface Segregation in Cu–Pt Nanoalloys: The Synergetic Roles in the Formation of Multishell Structures, *J. Phys. Chem. C*, 2015, **119**, 21515–21527.
43 T. Abe, B. Sundman and H. Onodera, Thermodynamic Assessment of the Cu–Pt System, *J. Phase Equilibria Diffus.*, 2006, **27**, 5–13.
44 Z. W. Lu, S.-H. Wei, A. Zunger, S. Frota-Pessoa and L. G. Ferreira, First-Principles Statistical Mechanics of Structural Stability of Intermetallic Compounds, *Phys. Rev. B: Condens. Matter Mater. Phys.*, 1991, **44**, 512–544.
45 A. F. Wells, *Structural Inorganic Chemistry*, Clarendon Press, Oxford, 5th edn, 1984.
46 J. Tang, L. Deng, H. Deng, S. Xiao, X. Zhang and W. Hu, Surface Segregation and Chemical Ordering Patterns of Ag–Pd Nanoalloys: Energetic Factors, Nanoscale Effects, and Catalytic Implication, *J. Phys. Chem. C*, 2014, **118**, 27850–27860.
47 J. M. Rahm and P. Erhart, Understanding Chemical Ordering in Bimetallic Nanoparticles from Atomic-Scale Simulations: The Competition between Bulk, Surface, and Strain, *J. Phys. Chem. C*, 2018, **122**, 28439–28445.
48 L. Deng, X. Liu, X. Zhang, L. Wang, W. Wei Li, M. Song, J. Tang, H. Deng, S. Xiao and W. Hu, Intrinsic Strain-Induced Segregation in Multiply Twinned Cu–Pt Icosahedra, *Phys. Chem. Chem. Phys.*, 2019, **21**, 4802–4809.
49 J. Pirart, A. Front, D. Rapetti, C. Andreazza-Vignolle, P. Andreazza, C. Mottet and R. Ferrando, Reversed size-dependent stabilization of ordered nanophases, *Nat. Commun.*, 2019, **10**, 1982.
50 N. Danielis, L. Vega, G. Fronzoni, M. Stener, A. Bruix and K. M. Neyman, AgPd, AuPd, and AuPt Nanoalloys with Ag- or Au-rich Compositions: Modeling Chemical Ordering and Optical Properties, *J. Phys. Chem. C*, 2021, **125**, DOI: 10.1021/acs.jpcc.1c04222.
51 S. Liu, Z.-J. Zhao, C. Yang, S. Zha, K. M. Neyman, F. Studt and J. Gong, Adsorption Preference Determines Segregation Direction: A Shortcut to More Realistic Surface Models of Alloy Catalysts, *ACS Catal.*, 2019, **9**, 5011–5018.
52 Y. Lykhach, S. M. Kozlov, T. Skála, A. Tovt, V. Stetsovych, N. Tsud, F. Dvořák, V. Johánek, A. Neitzel, J. Mysliveček, S. Fabris, V. Matolín, K. M. Neyman and J. Libuda, Counting Electrons on Supported Nanoparticles, *Nat. Mater.*, 2016, **15**, 284–288.
53 F. Viñes and A. Görling, Explaining Cu@Pt Bimetallic Nanoparticles Activity Based on NO Adsorption, *Chem. – Eur. J.*, 2020, **26**, 11478–11491.
54 Y. Suchorski, S. M. Kozlov, I. Bespalov, M. Datler, D. Vogel, Z. Budinska, K. M. Neyman and G. Rupprechter, The Role of Metal/Oxide Interfaces for Long-Range Metal Particle Activation during CO Oxidation, *Nat. Mater.*, 2018, **17**, 519–522.
55 R. Ferrando, A. Fortunelli and G. Rossi, Quantum Effects on The Structure of Pure and Binary Metallic Nanoclusters, *Phys. Rev. B: Condens. Matter Mater. Phys.*, 2005, **72**, 085449.
56 D. Cheng, W. Wang and S. Huang, The Onion-Ring Structure for Pd–Pt Bimetallic Clusters, *J. Phys. Chem. B*, 2006, **110**, 16193–16196.
57 D. Cheng, W. Wang, S. Huang and D. Cao, Atomistic Modeling of Multishell Onion-Ring Bimetallic Nanowires and Clusters, *J. Phys. Chem. C*, 2008, **112**, 4855–4860.
58 C. D. Feldt, R. Moreira, E. Meyer, P. Clawin, W. Riedel, T. Risse, L. Moskaleva, W. Dononelli and T. Klüner, CO Adsorption on Au(332):Combined Infrared Spectroscopy and Density Functional Theory Study, *J. Phys. Chem. C*, 2019, **123**, 8187–8197.
59 K. Tran and Z. W. Ulissi, Active Learning across Intermetallics to Guide Discovery of Electrocatalysts for CO_2 Reduction and H_2 Evolution, *Nat. Catal.*, 2018, **1**, 696–703.